The Astrophysical Journal, 711:959–973, 2010 March 10 doi:10.1088/0004-637X/711/2/959
© 2010. The American Astronomical Society. All rights reserved. Printed in the U.S.A.

DEPENDENCE OF INNER ACCRETION DISK STRESS ON PARAMETERS: THE SCHWARZSCHILD CASE

Scott C. Noble[1], Julian H. Krolik[2], and John F. Hawley[3]
[1] Center for Computational Relativity and Gravitation, School of Mathematical Sciences, Rochester Institute of Technology, 78 Lomb Memorial Drive, Rochester, NY 14623, USA; scn@astro.rit.edu
[2] Physics and Astronomy Department, Johns Hopkins University, Baltimore, MD 21218, USA; jhk@jhu.edu
[3] Department of Astronomy, University of Virginia, Charlottesville, VA, USA; jh8h@virginia.edu
Received 2009 November 13; accepted 2010 January 26; published 2010 February 19

ABSTRACT

We explore the parameter dependence of inner disk stress in black hole accretion by contrasting the results of a number of simulations, all employing three-dimensional general relativistic MHD in a Schwarzschild spacetime. Five of these simulations were performed with the intrinsically conservative code HARM3D, which allows careful regulation of the disk aspect ratio, H/R; our simulations span a range in H/R from 0.06 to 0.17. We contrast these simulations with two previously reported simulations in a Schwarzschild spacetime in order to investigate possible dependence of the inner disk stress on magnetic topology. In all cases, much care was devoted to technical issues: ensuring adequate resolution and azimuthal extent, and averaging only over those time periods when the accretion flow is in approximate inflow equilibrium. We find that the time-averaged radial dependence of fluid-frame electromagnetic stress is almost completely independent of both disk thickness and poloidal magnetic topology. It rises smoothly inward at all radii (exhibiting no feature associated with the innermost stable circular orbit, ISCO) until just outside the event horizon, where the stress plummets to zero. Reynolds stress can also be significant near the ISCO and in the plunging region; the magnitude of this stress, however, depends on both disk thickness and magnetic topology. The two stresses combine to make the net angular momentum accreted per unit rest mass 7%–15% less than the angular momentum of the ISCO.

Key words: accretion, accretion disks – black hole physics – magnetohydrodynamics (MHD) – radiative transfer

1. INTRODUCTION

At the very beginning of accretion disk studies, their overall properties were analyzed by applying the constraints of energy and angular momentum conservation to the simplest reasonable approximation to their structure: they were assumed to be time-steady and axisymmetric, and any internal vertical structure was integrated over (Novikov & Thorne 1973; Shakura & Sunyaev 1973; Page & Thorne 1974). The equation of energy conservation can be closed by counting the energy carried by photons to infinity, but no such ready closure exists for the angular momentum equation; angular momentum can be conserved for *any* rate of angular momentum transport through the disk provided it does not vary with radius. Consequently, it was necessary to guess the angular momentum flux in order to complete the solution. A convenient way to parameterize this guess is in terms of the net angular momentum accreted onto the black hole per accreted rest mass, $j_{\rm net}$. The choice made by the original papers, and still widely used today, is to suppose that no stresses act on the flow from the innermost stable circular orbit (ISCO) inward to the event horizon; if so, $j_{\rm net} = u_\phi({\rm ISCO})$, the orbital angular momentum of a test particle at the last stable orbit (here u_μ is the covariant four-velocity).

However, this was never more than a heuristic guess. As remarked by Thorne (1974), although the zero-stress boundary condition is plausibly motivated by hydrodynamic reasoning—the inertia of matter inside the ISCO should always be much less than that in the stable-orbit portion of the disk outside the ISCO—it might well be invalid if magnetic fields are important. In fact, one of the crucial things we have learned in the years since the 1970s is that magnetic fields are, in fact, essential to accretion due to the presence of the magnetorotational instability (MRI; Balbus & Hawley 1998). On that basis, this traditional boundary condition has been questioned (Krolik 1999b; Gammie 1999), and a number of numerical simulations of global disks (Hawley & Krolik 2001, 2002; Reynolds & Armitage 2001; Machida & Matsumoto 2003; Gammie et al. 2004; Krolik et al. 2005) have demonstrated that magnetic stresses near the ISCO and in the plunging region can be sizable.

On the other hand, it has also been suggested that the magnitude of these inner-disk stresses may be a function of disk parameters, notably its thickness. This was the result, for example, of an argument based on a hydrodynamic model with constant sound speed (Afshordi & Paczyński 2003). Parameterizing the disk thickness in terms of the ratio of its density scale height H to radial position r, Reynolds & Fabian (2008) found that the plunging region stress in a pseudo-Newtonian MHD simulation with $H/R = 0.05$ was rather smaller than in the analogous simulations of Hawley & Krolik (2001, 2002) in which H/R was 2–3 times larger.[4] Similarly, Shafee et al. (2008) found that for a disk with $H/R \simeq 0.06$–0.08 simulated with three-dimensional MHD in a Schwarzschild metric, the stress in the plunging region was significantly smaller than had been found in other simulations with aspect ratios a few times larger computed with different codes and somewhat different physical assumptions.

It is the goal of this paper to explore how the inner disk stress depends on parameters, particularly disk thickness, but also magnetic geometry. To test the former dependence, we have performed a new series of fully general relativistic three-dimensional MHD simulations with aspect ratios $H/R \simeq 0.06$, $\simeq$0.10, and $\simeq$0.17, all computed with the same code in the Schwarzschild metric and using appropriately scaled initial conditions. To explore the latter, we review results from previous relativistic disk simulations and, in particular, make detailed use of data from two previously reported simulations using a

[4] We also use R to represent the radial coordinate, i.e., $r = R$.

Schwarzschild spacetime. The disks in these two simulations had almost identical thickness, but in one case the initial magnetic field was a set of nested dipolar loops, while in the other the initial field was entirely vertical. Before presenting the results of these simulations, we will also discuss the importance of a number of technical considerations—particularly having to do with spatial resolution and the establishment of inflow equilibrium—to obtaining meaningful results.

2. SIMULATION DETAILS

The new simulations reported here were made using the code HARM3D, an intrinsically conservative method to solve the equations of three-dimensional MHD in an arbitrary metric. This new code is described in Noble et al. (2009); see also Gammie et al. (2003) for a description of the earlier axisymmetric version HARM, and Noble et al. (2006) for additional details on the primitive variable solver. We employ the same methodology as before, with only a few exceptions. In the following summary of this code's techniques, we emphasize those points that are different from the previous description or particular to the simulations discussed in this paper.

One of the principal aims of the present work is to study the influence of disk thickness H on the stress at the ISCO. We define it as the density moment in the coordinate frame

$$H \equiv \int d\theta d\phi \sqrt{-g}\, \rho \sqrt{g_{\theta\theta}} |\theta - \pi/2| \Big/ \int d\theta d\phi \sqrt{-g} \rho, \quad (1)$$

where $g_{\mu\nu}$ is the metric, g is the determinant of the metric, and ρ is the rest-mass density. When the density profile follows a Gaussian distribution with standard deviation H_G, $H = \sqrt{2/\pi} H_G = 0.798 H_G$. As in Noble et al. (2009), we regulate the thickness by cooling bound portions of the disk when the local temperature is greater than some target temperature $T_*(r)$. In terms of intensive quantities, bound matter satisfies $(\rho + u + P)\, u_t > -\rho$ and gas has temperature above the target when $(\Gamma - 1)\, u/\rho > T_*$; here, P is the gas pressure, u is the internal energy density, u_μ is the fluid's four-velocity, and Γ is the adiabatic index of the equation of state: $P = (\Gamma - 1)\, u$. The relativistic enthalpy $h \equiv 1 + (u + P)/\rho$. We set $\Gamma = 5/3$ throughout. The optically thin cooling function is implemented by modifying the stress-energy conservation equation to include a sink term: $\nabla_\mu T^{\mu\nu} = -\mathcal{L} u^\nu$.

The fluid-frame emissivity, $\mathcal{L}$, and T_* are designed so as to keep the density scale height at the desired value. The emissivity is the same as before but we slightly modified T_* to include a neglected relativistic correction. The new target temperature is

$$T_* = \frac{\pi}{2} \frac{R_z(r)}{r} \left[\frac{H(r)}{r} \right]^2, \quad (2)$$

where R_z is the relativistic correction to the vertical component of gravity (Abramowicz et al. 1997; Krolik 1999a):[5]

$$R_z(r) = \frac{1}{r} \left[l_k^2 - a^2 \left(\epsilon_k^2 - 1 \right) \right]. \quad (3)$$

Here, l_k and ϵ_k are the specific angular momentum (u_ϕ) and energy (u_t) of circular time-like geodesics in the equator of a black hole with spin parameter a. For $r < r_{\rm ISCO}$, l_k and ϵ_k remain at their ISCO values.

[5] Note that Equation (3) corrects Equation (7.43) of Krolik (1999a), which propagated a typographical error in Abramowicz et al. (1997).

All of the new simulations were performed in a Schwarzschild spacetime ($a = 0$) described in terms of Kerr–Schild coordinates and run for durations of 12000 M–15000 M (in our units, $G = c = 1$, so that both time and distance have units M, the mass of the central black hole). In all cases, the initial condition was a hydrostatic torus, but we examined two varieties of this state: in one the radial coordinate of the pressure maximum $r_{p_{\rm max}} = 35M$ and the inner edge $r_{\rm in} = 20\, M$; in the other, $r_{p_{\rm max}} = 25\, M$ and $r_{\rm in} = 15\, M$. The former set of parameters were chosen to match those of Shafee et al. (2008), the latter to match those of De Villiers et al. (2003). In the remainder of this paper, we will refer to the former set as "HR" and to the latter set as "LR" because the grid schemes used for the former were in general higher resolution than for the latter. The q parameter determines the angular velocity profile in the initial torus ($\Omega \propto r^{-q}$). The choice of q along with the choice of pressure maximum and inner torus edge determines the characteristic vertical thickness of the initial torus. For LR simulations, q was set to 1.68, while for HR, q was determined by requiring the initial disk's thickness at $r = r_{p_{\rm max}}$ to be equal to the run's target thickness. To study the effect of different disk thicknesses, we ran HR simulations for three different target temperatures, chosen to make $H/R \simeq 0.05$, 0.08, and $\simeq$0.16; these were designated "Thin," "Medium," and "Thick," respectively. We ran only LR simulations for the Thin and Medium cases. Finally, in all five simulations, the initial magnetic field consisted of dipole poloidal loops, with field lines following density contours, and with amplitude set such that the mean initial plasma $\beta = 100$. Turbulence was seeded by adding random perturbations to u at the 1% level.

Boundary conditions were imposed through assignment of primitive variables in ghost zones; the primitive variables are ρ, u, v^i (spatial velocity components), and B^i (magnetic field components). The v^i are spatial components of the four-velocity as seen by observers in the Zero Angular Momentum Observer (ZAMO) frame; the B^i are the spatial components of the magnetic field as represented in the Maxwell field tensor, i.e., $B^i \equiv {}^*F^{it}/\sqrt{4\pi}$. Outflow boundary conditions were taken both at $r = r_{\rm max}$ and $r = r_{\rm min}$: all primitive variables are extrapolated at zeroth order into the ghost zones, but u^r is set to zero—and v^i recalculated—whenever it points into the domain. In order to prevent numerical boundary effects from propagating outside the trapped surface, we chose $r_{\rm min}$ so that the numerical domain extended 5–25 cells inside the event horizon. When there was a cutout around the polar axis (see grid details below), reflective boundary conditions are imposed on the perpendicular vector components while all other quantities are extrapolated beyond the cutout with zeroth-order accuracy. If the cutout size is negligible, ghost zone values are set so as to make the variables continuous across the pole. In order to gain a factor of 4 in computer resources, we simulated only a quarter of the azimuthal domain, employing periodic boundary conditions linking $\phi = 0$ and $\phi = \pi/2$.

Adequate resolution throughout the accretion flow and throughout the duration of the simulation is vital to ensure quantitative accuracy, particularly for magnetic effects. To explore the consequences of resolution effects, we used two different grid schemes, one for HR and the other for LR. Both were designed with an eye toward satisfying several conflicting criteria. On the one hand, it is always desirable to have the finest feasible spatial resolution. Toward that end, the grid scheme should provide at least several dozen cells per scale height on either side of the equatorial plane, and the poloidal cell aspect ratio should never be too large. In addition, the number of cells within a

Table 1
Simulation Parameters

Name	Target H/R	Cell Count[a]	θ Grid	ξ	θ_c	θ_0	s	Cell Shape[b] ($\theta = \pi/2$)	Cell Shape[b,c] ($\theta = 2H/R$)	$\Delta\theta_{\rm min}/10^{-3}$
ThinHR	0.05	$912 \times 160 \times 64$	(6)	0.93	$\pi \times 10^{-15}$	...	...	3.0:1:17	0.48:1:2.7	1.4
ThinLR	0.05	$192 \times 192 \times 64$	(5)	0.49	10^{-15}	0	π	71:1:74	2.0:1:2.1	0.33
MediumHR	0.08	$512 \times 160 \times 64$	(6)	0.93	$\pi \times 10^{-15}$	...	...	5.8:1:17	0.43:1:1.3	1.4
MediumLR	0.08	$192 \times 192 \times 64$	(5)	0.35	0.083	θ_c	0.95	5.1:1:5.3	2.7:1:2.7	4.7
ThickHR	0.16	$348 \times 160 \times 64$	(6)	0.76	0.094	...	...	3.0:1:5.3	0.87:1:1.4	4.6
KD0c	... [d]	$192 \times 192 \times 64$	(Hawley & Krolik 2006)		0.045π			2.4:1:2.3	2.1:1:1.9	11
VD0	... [d]	$256 \times 256 \times 64$	(Beckwith et al. 2009)		0.01π			2.7:1:2.9	2.3:1:2.4	8.4

Notes.
[a] $N_r \times N_\theta \times N_\phi$.
[b] $\sqrt{g_{rr}}\Delta r : \sqrt{g_{\theta\theta}}\Delta\theta : \sqrt{g_{\phi\phi}}\Delta\phi$.
[c] Values of H/R used here are the actual time-averaged quantities specified in Table 2.
[d] Unregulated scale height.

wavelength of the fastest growing MRI mode should only occasionally fall below $\simeq$6, the minimum resolution level at which the mode grows at the correct rate (Sano et al. 2004). On the other hand, to fit within existing computational resources, the total cell count cannot be too great nor the time step too small.

Each run used a unique discretization tailored to its particular target thickness. HARM3D accomplishes nonuniform discretization through continuous coordinate transformations from an underlying uniform mesh. The finite volume equations are discretized with respect to points uniformly distributed in coordinates, x^μ, which are placed nonuniformly in the spherical coordinate system r, θ, and ϕ. The center of cell C_{ijk} is located at $(x^1_{i+1/2}, x^2_{j+1/2}, x^3_{k+1/2})$, where $x^\mu_i \equiv x^\mu_0 + i\Delta x^\mu$ and Δx^μ is a cell's extent in the x^μ direction. We choose $t = x^0$, $\phi = x^3$, and

$$r_i = e^{x^1_i}, \tag{4}$$

so that $\Delta r/r$ is the same everywhere. For N_1 grid cells along the x^1 axis and minimum and maximum radii $r_{\rm min}$ and $r_{\rm max}$, $\Delta x^1 = \frac{1}{N_1}\log\left(\frac{r_{\rm max}}{r_{\rm min}}\right)$.

The relationship between x^2 and θ is determined differently in the HR and LR simulations. In the LR group, we follow previous work (e.g., Gammie et al. 2003; Noble et al. 2007, 2009), but introduce a "cutout" or excised region around the polar axis

$$\theta(x^2) = \theta_c + (\pi - 2\theta_c)\,x^2 + \xi\,\sin\left[2\left(\theta_0 + s x^2\right)\right], \tag{5}$$

where θ_c is the approximate size of the cutout, θ_0 and s control the nonlinearity of the transformation, and ξ is the amplitude of the nonlinear part. One drawback to this transformation is that if one tries to place a majority of the points within the first two scale heights from the equator, the minimum $\Delta\theta$, which is always found at $\theta = \pi/2$, is so small that the time step is prohibitively small.

In the HR simulations, we follow the method of Shafee et al. (2008), adapted here to include a cutout. In this method, the sinusoidal nonlinear term is replaced with a polynomial

$$\theta(x^2) = \frac{\pi}{2}\left[1 + (1-\xi)\left(2x^2 - 1\right) + \left(\xi - \frac{2\theta_c}{\pi}\right)\left(2x^2 - 1\right)^n\right], \tag{6}$$

where n is a positive odd integer, θ_c is the size of the excised region, and ξ is still the relative amplitude of the nonlinear term. Note that near the equator, where most of the points are located, the linear term dominates and $\Delta\theta(x^2)$ is nearly uniform. Periodicity of $\theta \in [0, 2\pi]$ is ensured by making x^2 a periodic triangle function over $[0, 2]$. We set $n = 9$ whenever Equation (6) is used for the runs presented here.

Because gridscale dissipation scales with the ratio of cell dimension to the length scale on which physical quantities vary, cells that are far from cubical may have effective dissipation properties that are anisotropic. This might produce unphysical results because physical dissipation mechanisms are unlikely to have this property. For this reason, we strive to limit the degree of anisotropy in our cell shapes, although cells longer by factors of a few in the ϕ-coordinate than in the others are acceptable because orbital shear tends to draw out features in the azimuthal direction. At the same time, it is important, especially for small H/R simulations, to make the θ-direction cell thickness small enough to put an adequate number of cells within a vertical scale height. Achieving these conflicting goals is easier with the HR grid scheme than with the LR scheme (as illustrated by the data in Table 1). Our HR runs use grids with $\Delta r : r\Delta\theta \simeq 2 : 1$ while achieving at least 60 cells per scale height. In LR simulations, although the aspect ratios are acceptable at an altitude $\sim H$ away from the equatorial plane, they are rather extreme close to the plane, and—of these runs—only ThinLR has a comparable number of cells per vertical scale height to HR runs (see Table 2).

The time step $\Delta t = \Delta x^0$ is set equal to 0.8 times the shortest cell crossing time for the fastest MHD characteristic from the previous time step.

The defining parameters of the simulations are collected in Table 1. In the first column we state the names of the runs. The body of the name corresponds to the disk thickness, the suffix refers to the grid resolution. The target aspect ratio H/R is shown in the second column. Note that the "radius" to which the scale height is compared is the radial coordinate, which is not identical to a length in any frame of reference. Since we regulate the temperature, not H directly, the actual value will not in general exactly coincide with the target. The observed value of H/R is given in Table 2, and is obtained by averaging over the time interval shown in its last column (whose origin is discussed in Section 3.2) and radially averaging from the ISCO ($r = 6M$) to the run's $r_{p_{\rm max}}$. The third column, cell count, is self-explanatory. Columns 4–8 define the poloidal discretization. Columns 9 and 10 state the typical cell aspect ratio at the equator and at two scale heights from the equator, and Column 11 lists the size of the smallest poloidal extent ($\Delta\theta$) of a cell, which always occurs at $\theta = \pi/2$.

Table 2
Simulation Results

Simulation	Actual $\langle H/R\rangle$[a]	$j_{\rm net}$	$N_{\rm cells}(\lvert z\rvert < H/R)$[b]	$\Delta t_{\rm ave}/\left(10^3 M\right)$
ThinHR	0.061	3.13	81	10–15
ThinLR	0.085	3.07	60	4.5–11.5
MediumHR	0.10	3.08	103	5–12.5
MediumLR	0.091	3.10	35	5–8
ThickHR	0.17	2.93	74	8–13.66
KD0c	0.13[c]	3.21	24	4–10
VD0	0.14	3.06	32	14–20

Notes.
[a] Average of $H(r,t)/R$ in time (over each run's $\Delta t_{\rm ave}$) and in radius (weighted uniformly with respect to $\log r$) from $r_{\rm ISCO}$ to $r_{p_{\rm max}}$.
[b] Number of cells per scale height averaged with respect to $\log r$, i.e., $\int \mathcal{N}(r)\, d\log r / \int d\log r$, where $\mathcal{N}(r)$ is the number of cell widths within $\theta \in [\pi/2 - H(r)/R\,,\ \pi/2 + H(r)/R]$ and the bounds of integration are $r \in [r_{\rm hor}, r_{p_{\rm max}}]$.
[c] Averaging period used here was $8000M$–$10000M$ instead of $\Delta t_{\rm ave}$ because only these data were saved.

We will also analyze two older simulations, both done with the general relativistic three-dimensional MHD code GRMHD (originally described in De Villiers & Hawley 2003). Both began with the gas in a hydrostatic torus. The first, called "KD0c," was described in Hawley & Krolik (2006) and had initial conditions similar to the LR models presented here. The other, called "VD0" and analyzed in Beckwith et al. (2009), began with a constant intensity vertical magnetic field filling the annulus $35M \leqslant r \leqslant 55M$ and running through an initial torus with a pressure maximum at $r = 40M$. Unlike the HARM3D simulations, there was no explicit cooling function included. Rather, the internal energy equation was evolved and the only heating included was shock heating captured by an artificial viscosity term. The resulting H/R values are given in Table 2 and, in terms of the descriptive terms used here, qualify these simulations as "thick."

3. QUALITY AND CONSISTENCY CHECKS

We are investigating the stress at the ISCO in a steady state accretion disk with a focus on the role of vertical scale height. To model the accretion disk system, we use the equations of conservative ideal MHD along with an ad hoc cooling function to control the disk's thickness. We can, however, run only a discrete set of simulations, evolved for a limited time from particular initial conditions, using a grid with restricted spatial extent and modest resolution. The conclusions we obtain must be assessed within the context of the limitations of those simulations.

In this section, we consider the effects of some of these numerical limitations by developing several quantitative diagnostics to measure their possible significance. We begin by considering the adequacy of the grid resolution, and then look at how closely the inner disk approximates a statistical steady state. Finally, since this study focuses on the effect of disk scale height for the ISCO stress, we check to see how well we are able to control that variable.

3.1. Resolution

Inadequate resolution can cause a number of numerical artifacts. For example, the growth rate of the underlying MRI can be suppressed if there are fewer than $\simeq$6 zones within a wavelength of the fastest growing mode (Sano et al. 2004). The MRI produces turbulence, but only a small range in wavenumber space can be captured, possibly distorting the properties of that turbulence. The rate at which nonlinear mode–mode couplings transfer energy from large-scale motions to small may be altered. And resolution that is too coarse may drive an artificially large rate of magnetic numerical dissipation.

Unfortunately, there is no a priori standard by which we can measure whether a given grid scheme either exhibits excessive magnetic reconnection or improperly evaluated nonlinear mode couplings. Only through a numerical convergence test, in which increasingly better resolved simulations give quantitatively consistent results, can one demonstrate that resolution artifacts are not influencing the outcomes. As a practical matter, however, one carries out simulations such as these at the highest feasible resolution. Lower resolution simulations might provide some information, but with the computational resources at our disposal it has not been possible to improve sufficiently upon the resolution used in the production simulations to establish formal convergence.

It is possible, however, to check whether the grid resolution satisfies certain physical criteria, such as having a sizable number of cells per vertical scale height and sufficient cells across the fastest growing MRI wavelength that the linear growth of these modes is correctly described. Both criteria may be met in the initial conditions, but the data must be examined throughout the relevant volume (the main disk body) and for the duration of the simulation to ensure that they continued to be satisfied.

Data on the mean number of cells per scale height are displayed in Table 2. There we see that in all the HR simulations, there were at least $\simeq$40 cells per scale height. ThinLR was almost as well resolved as the HR simulations with respect to this measure, with 30 cells per H. MediumLR has somewhat fewer cells per scale height, $\simeq$18, but even with this number should still be able to resolve well dynamics on the scale of a fraction of a scale height.

To quantify the quality of resolution of the MRI, we evaluated the parameter $Q \equiv \lambda_{\rm MRI}/\Delta z$, where both $\lambda_{\rm MRI}$ and Δz are computed in the fluid frame,

$$\lambda_{\rm MRI} \equiv \frac{1}{\sqrt{4\pi\rho}\,\Omega(r)} b_\mu \hat{e}^\mu_{(\theta)}, \tag{7}$$

and

$$\Delta z \equiv dx^\mu \hat{e}^{(\theta)}_\mu, \tag{8}$$

where $\hat{e}^\mu$ and $\hat{e}_\mu$ are contra- and co-variant tetrad systems in the local fluid frame, respectively. To assure ourselves that the simulations always satisfied this criterion, we created animations of Q with frames every $20M$ in time. In Figure 1, we show sample stills from the simulations ThinHR, ThinLR, MediumHR, and ThickHR, each exhibiting a vertical slice at fixed azimuthal angle. All of these simulations exhibited better than adequate resolution at all times: the typical number of cells across the fastest-growing mode in the disk body was $\gtrsim$ 20. Azimuthally averaged versions of the data shown in Figure 1 display ratios of fastest growing wavelength to cell size greater than 12 throughout the entire region within two scale heights of the equatorial plane. It is important to recognize, however, that even in a superbly resolved simulation there will always be the occasional region in which the local poloidal field strength is small simply because this is a chaotic system in which fields are free to have either sign.

The importance of Q comes from the requirement that the MRI maintain turbulence in the face of continual dissipation.

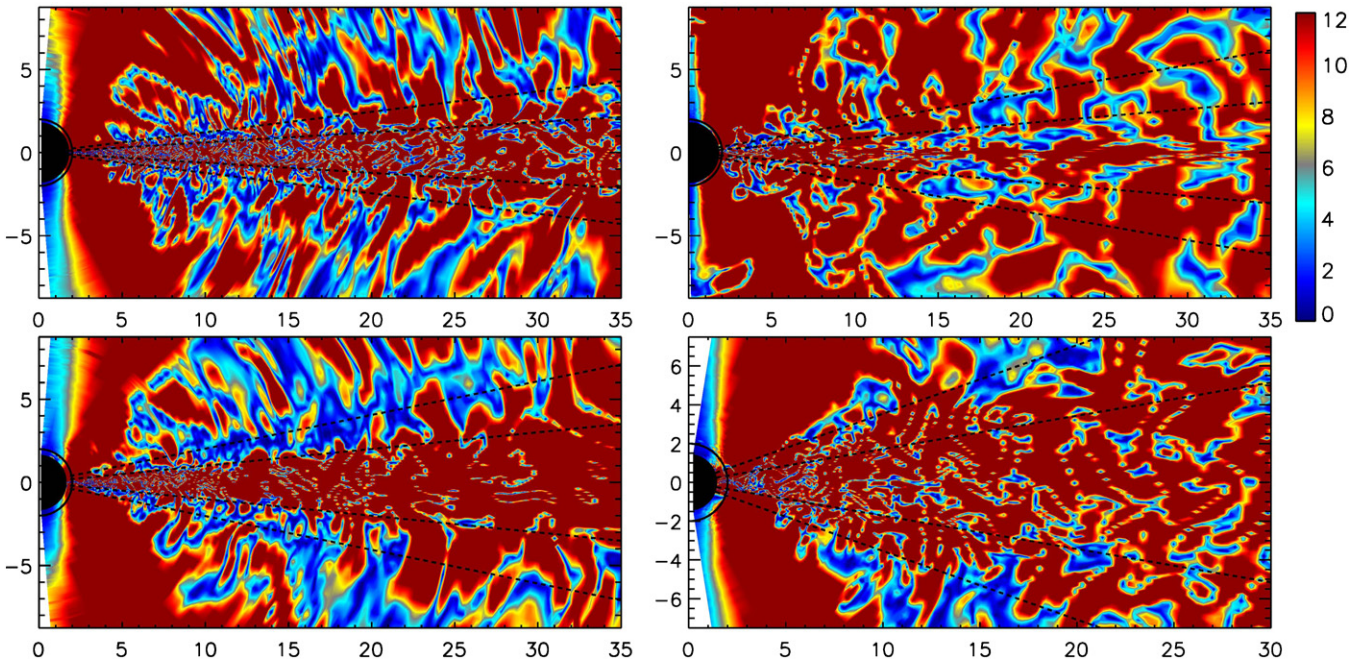

Figure 1. Sample data illustrating resolution of the MRI in simulation ThinHR (top left), ThinLR (top right), MediumHR (bottom left), and ThickHR (bottom right). In each case, the region shown is a poloidal slice at $\phi = \pi/4$. Regions with deep red color are well resolved; those in blue are poorly resolved. The dashed black lines show one and two scale heights from the midplane.

If the MRI growth rate is artificially reduced due to poor resolution,[6] and field amplification by MHD turbulence is too weak, the field strength can become increasingly anemic. Thus, it is possible for a simulation that began with ample cells per MRI wavelength to suddenly find itself under-resolved. The end result is a field that dies away and a cessation of accretion due entirely to inadequate resolution.

This appears to happen in the MediumLR simulation beginning at $t \simeq 9000M$. MediumLR demonstrates the utility of the resolution diagnostic. Figure 2 shows two stills, at times $6000M$ and $12000M$, from the resolution animation for this simulation. Initially well resolved, MediumLR becomes more poorly resolved as the field strength diminishes. As a result, the accretion rate also decays.

The two GRMHD simulations can be analyzed in similar fashion. By the standards of the HARM3D simulations, both have relatively few cells per scale height, only $\simeq$12–16, not quite as many as in MediumLR. We also show sample snapshots of Q in Figure 3, in each case showing the final time-step of the simulation. KD0c was performed several years ago, and we did not save enough snapshots to create an animation; of all those available (every $80M$ from $t = 8000M$ to $t = 10000M$), the one shown in Figure 3 appears to be the least well resolved. In fact, there is an indication of a secular worsening of resolution beginning at $t \simeq 9000M$. In the case of VD0, we possess more data and have confirmed that at no time was the resolution substantially poorer than shown here. As can be seen, in neither case was the resolution as good as in the best of the HARM3D simulations, although VD0 at its end point was better than KD0c at its.

3.2. Inflow Equilibrium

In the end, we hope to use these evolving simulations to describe time-steady accretion flows. Starting from our initial condition, this state can never be achieved at all radii because the angular momentum removed from accreting material will be transferred to matter at larger radius, causing that matter to move outward. Moreover, because only a fraction of the initial torus mass is accreted in the duration of the simulations, the radial surface density profile can relax to the one associated with inflow equilibrium only within a short distance outside the initial inner radius of the torus ($20M$ for HR, $15M$ for LR).

Nonetheless, it is possible to identify a period of time for which an approximate state of inflow equilibrium really does obtain over a reasonable dynamic range in radius, subject, of course, to the sorts of fluctuations that occur in statistically stationary turbulent systems. To identify that region in both time and space, we impose several tests relying on the conservation of mass and angular momentum. Whenever the disk is in inflow equilibrium, the radial fluxes of mass and angular momentum should be constant as a function of radius, but because of turbulent fluctuations, they are constant only in a time-averaged sense. The radial range of the equilibrium region is determined by the range over which the time-averaged values of these quantities are nearly constant. To identify the time periods in which equilibrium obtains, we consider the mass interior to several specific radii $M(< r; t)$ and the time dependence of the specific angular momentum accreted onto the black hole, $j_{\rm net}$. In inflow equilibrium, these should be roughly constant over time.

The mass interior to radius r is defined as the integral of the mass density over the computational volume from the horizon

[6] Although one generally expects poor resolution to limit the strength of the MRI turbulence, Fromang & Papaloizou (2007) found that for zero net magnetic flux unstratified shearing box experiments, increased resolution led to decreased turbulent stress, appearing to converge to zero as resolution increased. It now seems that this result arises from another numerical limitation, namely the lack of any length scale besides that of a grid zone. Both Shi et al. (2010) and Davis et al. (2009) find that convergence to a nonzero stress is recovered when vertical gravity is added.

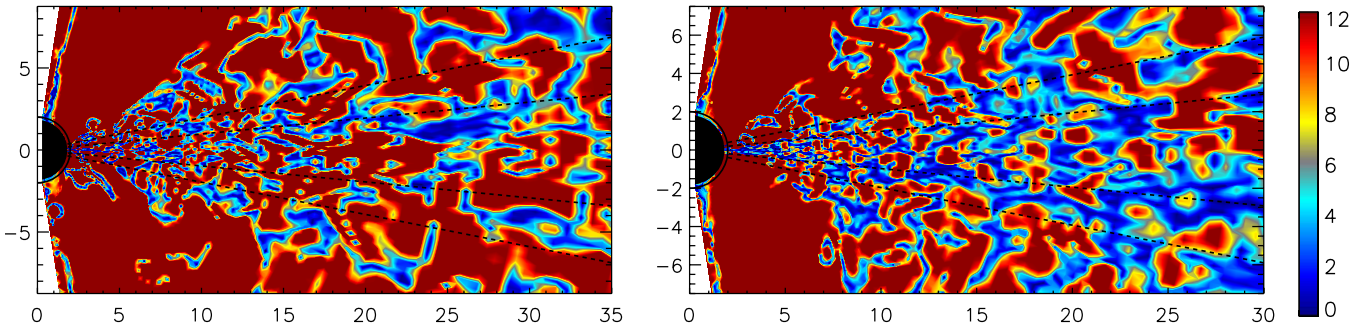

Figure 2. Sample data illustrating resolution of the MRI in simulation MediumLR while it was well resolved (left, at time $t = 6000M$) and after it became poorly resolved (right, at time $t = 12000M$). In both cases, the region shown is a poloidal slice. Regions with deep red color are well resolved; those in blue are poorly resolved. The dashed black lines show one and two scale heights from the midplane.

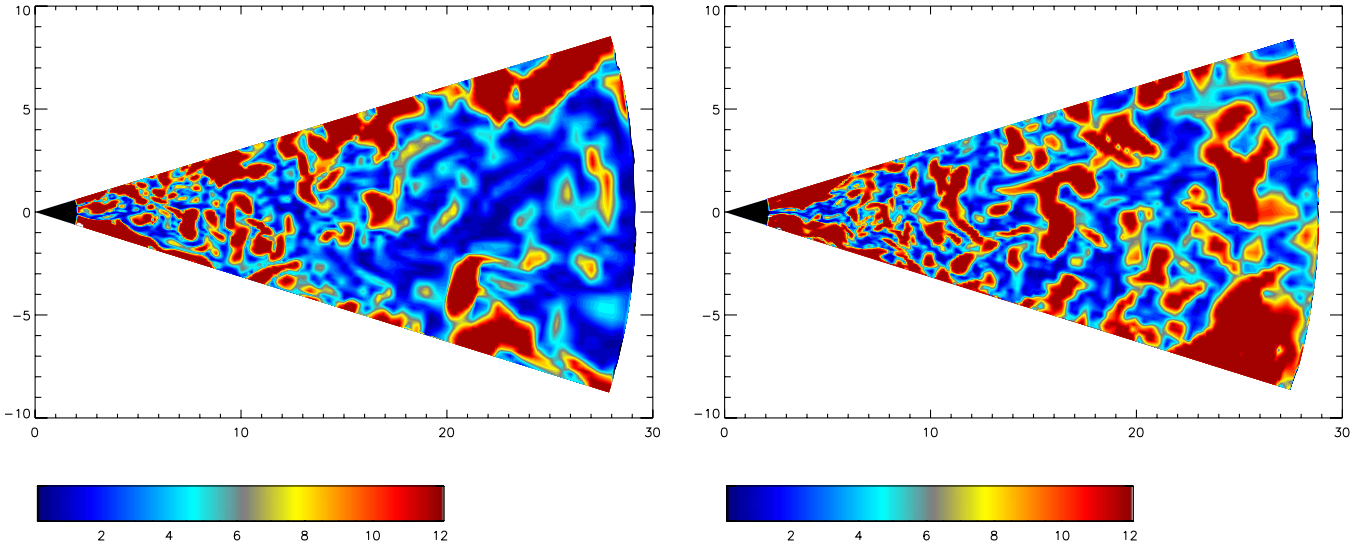

Figure 3. Sample data illustrating resolution of the MRI in simulation KD0c at its end time, $t = 10000M$ (left) and in simulation VD0 at its end time, $t = 20000M$ (right). In both cases, the region shown is a poloidal slice extending 0.3 rad, $\simeq 2H$, from the midplane.

to radial coordinate r, or

$$M(< r; t) \equiv \int_{r_{\rm hor}}^{r} dr'\, d\theta\, d\phi\, \sqrt{-g}\, \rho. \tag{9}$$

Thus, once inflow equilibrium is established, the mass within a given radius should stay the same, as the amount of mass entering from outside is matched by the mass accreted onto the black hole at the center.

Figures 4–6 display the history of mass inside $r = 10M$, $15M$, and $20M$ for each of the three disk aspect ratio categories studied. In all cases, at early times the mass in the disk grows as accretion from the initial torus fills in rings at smaller radii. Eventually, the mass-interior curves level off, signaling the approach to equilibrium with respect to this criterion. In the case of MediumLR, the mass in the inner disk declines at late times, a symptom of the diminution in the accretion rate which we attribute to the artificial decay of the magnetic field.

Similar data for the two GRMHD simulations are given in Figure 7. Both simulations reach inflow equilibrium with respect to this criterion, after $\simeq 3000M$ in the case of KD0c, after $\simeq 10000M$ in the case of VD0.

Another test of inflow equilibrium is provided by the history of the specific angular momentum accreted into the black hole, $j_{\rm net}$. This is determined by dividing the total angular momentum flux by the accretion rate

$$j_{\rm net}(r, t) \equiv \frac{\langle T^r{}_\phi \rangle}{\langle \rho u^r \rangle}, \tag{10}$$

where the brackets represent the shell integration of the bracketed quantity

$$\langle X \rangle \equiv \int d\theta\, d\phi\, \sqrt{-g}\, X. \tag{11}$$

The quantity $j_{\rm net}(r, t)$ will be constant in r where there is inflow equilibrium. If the accretion disk is truly in a statistically steady state in regard to its angular momentum flow, this quantity should exhibit no trends in time, varying only modestly due to fluctuations intrinsic to the turbulence. Figure 8 shows $j_{\rm net}(r_{\rm hor})$ as a function of time for the entire duration of each of the five new simulations. They display quite different behavior. Once accretion begins, $j_{\rm net}$ hardly varies in ThinHR. Although there are no secular trends in ThinLR after $t = 2000M$, there are two sharp drops, at $t = 4000M$ and $12000M$, and its fluctuations are in general rather larger than in ThinHR. The curve of $j_{\rm net}(t)$ in MediumHR is more or less flat after $t = 5000M$, but its fluctuations are almost as large as those in ThinLR. By contrast, $j_{\rm net}$ rises in a succession of steps in MediumLR, showing relatively brief periods of near-constancy. Finally, $j_{\rm net}(t)$ rises rapidly from the beginning of ThickHR until about $t = 8000M$, holding approximately steady from then until the end of the simulation at $13660M$.

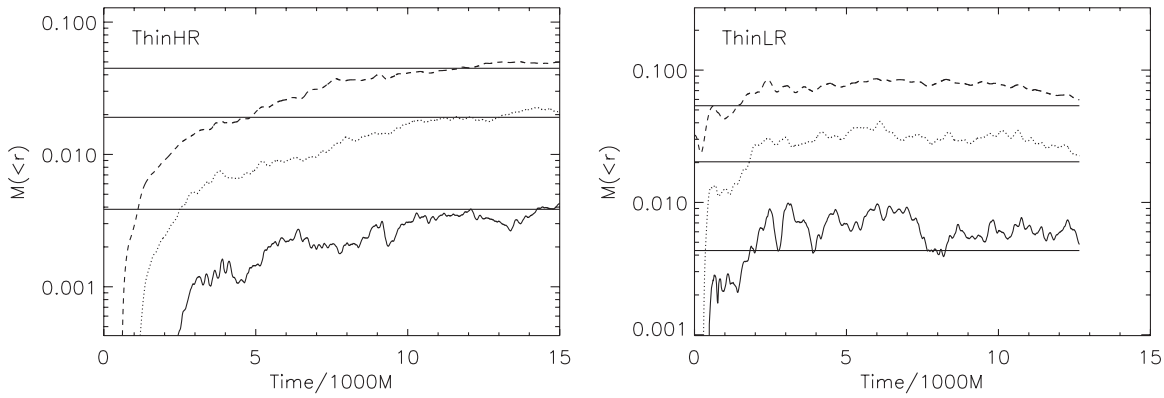

Figure 4. Mass (normalized to the initial total mass in the disk) inside $r = 10M$ (thick solid curve), $r = 15M$ (dotted curve), and $r = 20M$ (dashed curve) for the thin simulations. The three horizontal thin solid lines show 90% of the final mass for each of these radii. Left: HR. Right: LR.

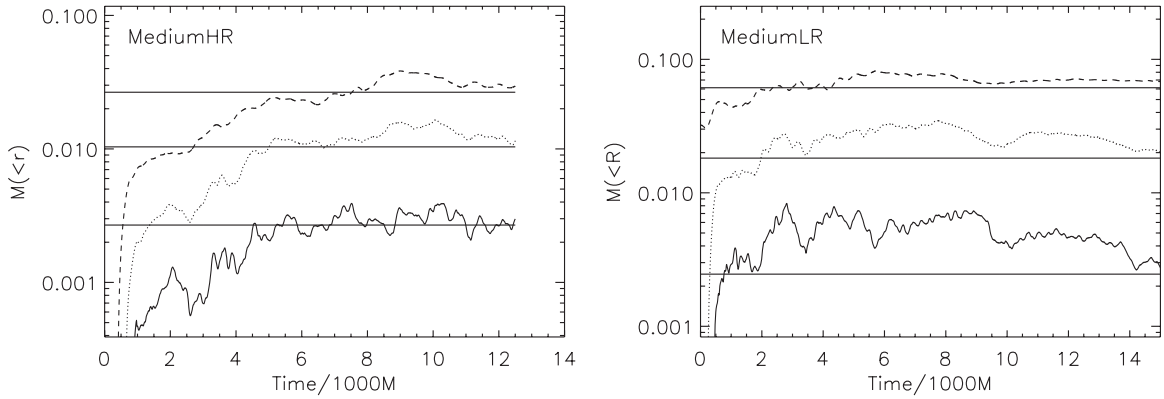

Figure 5. Mass (normalized to the initial total mass in the disk) inside $r = 10M$ (thick solid curve), $r = 15M$ (dotted curve), and $r = 20M$ (dashed curve) for the medium simulations. The three horizontal thin solid lines show 90% of the final mass for each of these radii. Left: HR. Right: LR.

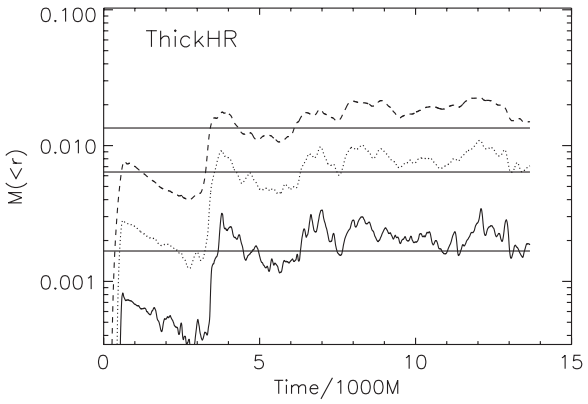

Figure 6. Mass (normalized to the initial total mass in the disk) inside $r = 10M$ (thick solid curve), $r = 15M$ (dotted curve), and $r = 20M$ (dashed curve) for the thick simulation. The three horizontal thin solid lines show 90% of the final mass for each of these radii.

The time dependence of $j_{\rm net}$ in MediumLR is instructive. Overall, especially after $10000M$, $j_{\rm net}$ rises toward u_ϕ(ISCO). As discussed in Section 3.1, the average number of grid zones per most unstable wavelength dropped in this simulation as the field weakened. Inadequate resolution leads to ever-weaker magnetic field which, in turn, results in a rise of the specific accreted angular momentum toward the ISCO value as the magnetic stress is reduced.

Figure 9 shows $j_{\rm net}$ for the GRMHD simulations KD0c and VD0. The zero net-flux simulation, KD0, shows no secular trend in this quantity after $4000M$, suggesting an inflow equilibrium. In VD0, on the other hand, the fluctuations in $j_{\rm net}$ are much stronger, and there also appears to be a rising trend from the beginning of the simulation up until $t \simeq 14000M$, after which the trend flattens out and the fluctuations begin to diminish.

Combining what we have seen in the mass-interior plots with those in the $j_{\rm net}$ histories, we define the averaging periods, $\Delta t_{\rm ave}$, for these simulations as the time when *both* criteria for inflow equilibrium are met. The results of this analysis are shown in the last column of Table 2. In two cases (MediumHR, ThickHR), the two tests single out the same periods; in one case (ThinHR), the mass-interior equilibrium period is a portion of the specific angular momentum equilibrium period; in four other cases (ThinLR, MediumLR, KD0c, VD0), only a part of the period that meets the mass-interior test is also in equilibrium according to the specific angular momentum test.

With the appropriate time-averaging period chosen, we can study how the time-averaged accretion rate varies with radius. Of the seven simulations, in only one (ThinHR) is the contrast in $\langle \dot{M} \rangle = \langle \rho u^r \rangle$ inside $r = 20M$ as much as 30%; in one (MediumLR) it is $\simeq$10%; in all the others (ThinLR, MediumHR, ThickHR, KD0c, VD0), it is no more than a few percent.

3.3. Scale-height Regulation

Finally, we examine the actual time-averaged scale heights achieved in the various simulations; these are shown in Figure 10. The scale-height regulation employed in the HARM3D simulations is quite successful at enforcing a fixed ratio H/R (except in the plunging region in ThickHR), but, as shown in Table 2, the actual value obtained can be different from

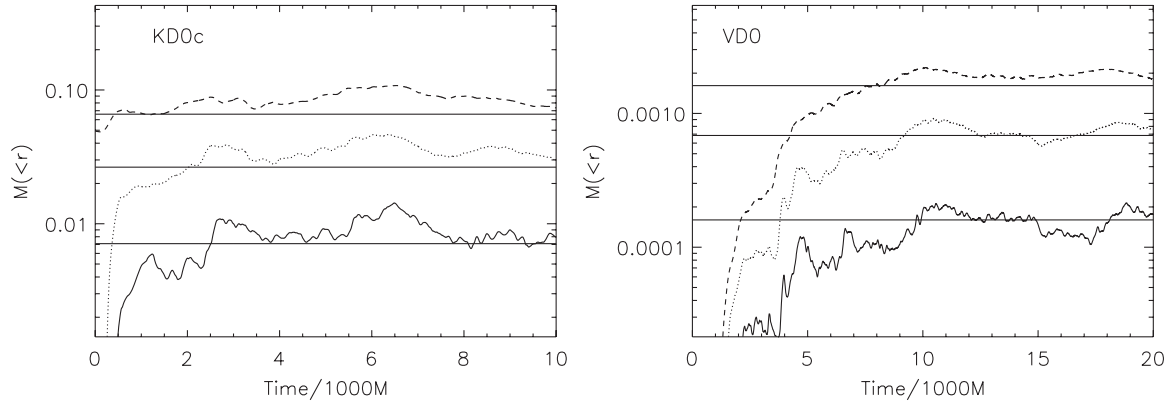

Figure 7. Mass interior to $r = 10M$ (thick solid curve), $r = 15M$ (dotted curve), and $r = 20M$ (dashed curve) for the two GRMHD simulations. The three horizontal thin solid lines show 90% of the final mass for each of these radii. Left: KD0c. Right: VD0.

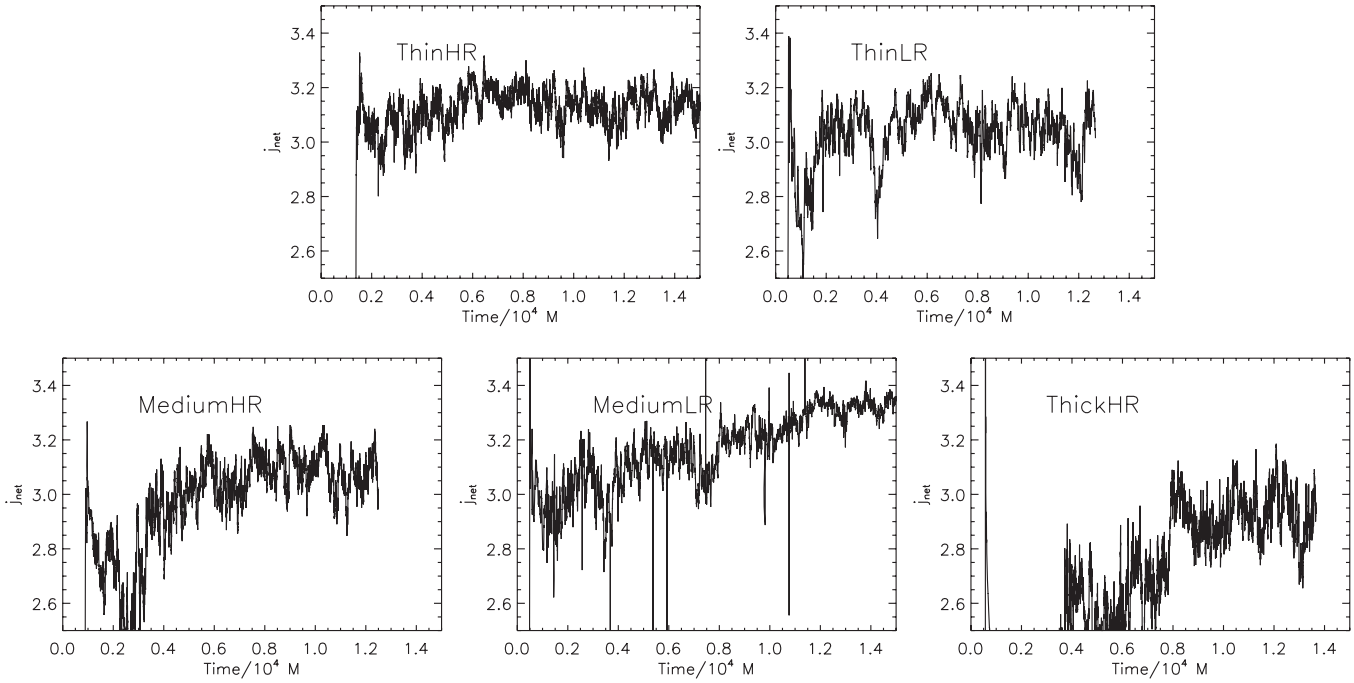

Figure 8. Net specific accreted angular momentum, $j_{\rm net}$, as a function of time in ThinHR (top left), ThinLR (top right), MediumHR (bottom left), MediumLR (bottom middle), and ThickHR (bottom right). Note that $u_\phi(\mathrm{ISCO}) = 3.464$ in Schwarzschild spacetime.

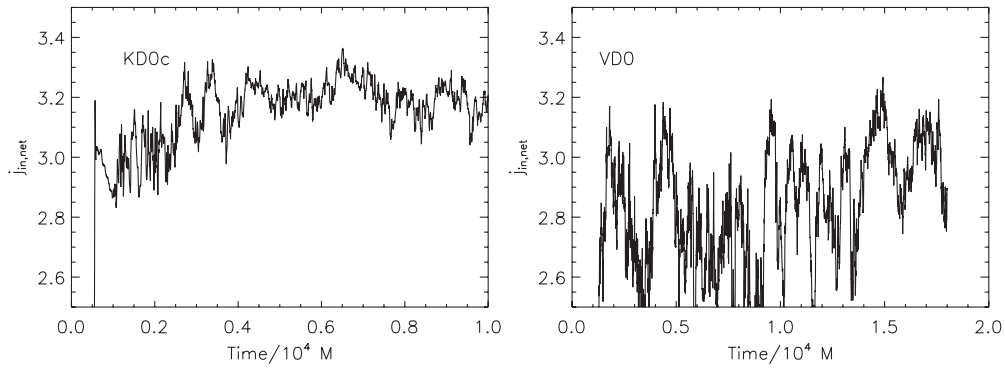

Figure 9. Net specific accreted angular momentum, $j_{\rm net}$, as a function of time in KD0c (left) and VD0 (right). Note that $u_\phi(\mathrm{ISCO}) = 3.464$ in Schwarzschild spacetime.

the target, $\simeq$20% greater in the cases of ThinHR, MediumHR, and MediumLR, but $\simeq$70% greater in the case of ThinLR. Part of this consistent offset can be attributed to magnetic support, and part to the fact that the temperature is typically slightly greater than the target. The large offset in ThinLR is a consequence of its initial condition, in which the gas was given a thickness almost twice as great as the target. Although its initial mean plasma β was 100, when cooling compresses the disk by a sizable factor, the magnetic field strengthens while the gas pressure falls. As a result, much of the disk mass of ThinLR outside a thin

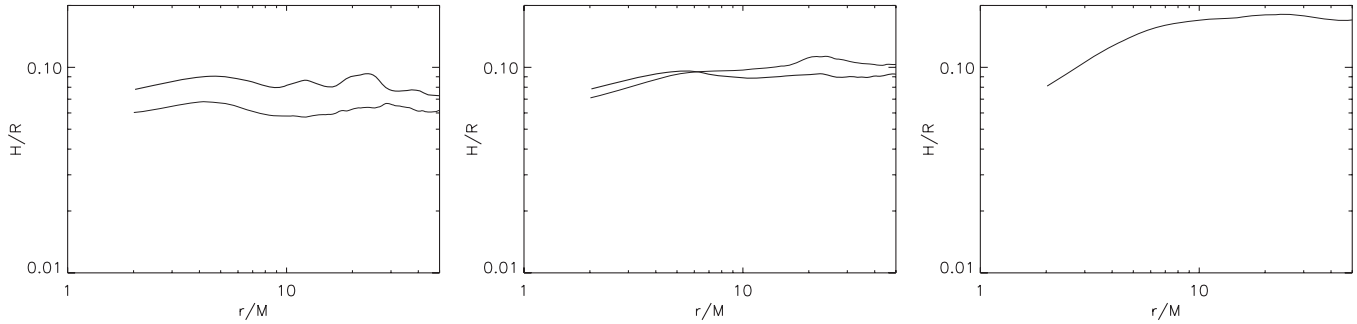

Figure 10. Time-averaged scale height as a function of radial coordinate for each of the HARM3D simulations. Left: ThinHR and ThinLR; center: MediumHR and MediumLR; right: ThickHR. In each case, the heavy curves correspond to HR and the light curves to LR.

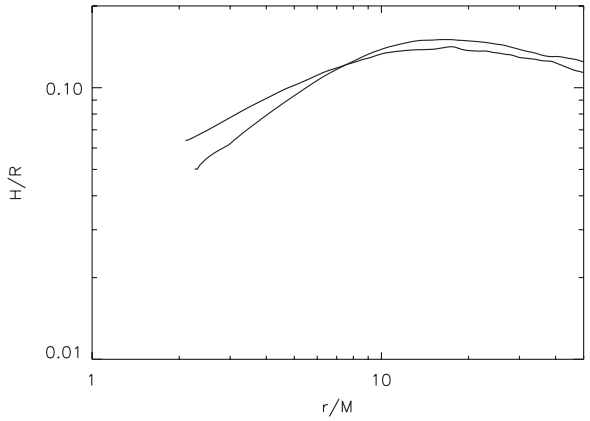

Figure 11. Time-averaged scale height as a function of radial coordinate for the two GRMHD simulations. The thick curve is the zero net-flux case, KD0c; the thin curve is the nonzero flux case, VD0.

midplane layer was supported magnetically, and its scale height was substantially increased beyond what its gas pressure alone could support. This fact emphasizes the importance of choosing initial conditions relatively close to the expected time-averaged state. Inside the ISCO, the aspect ratio decreases slightly because the inflow time is so short that the disk cannot maintain vertical hydrostatic equilibrium.

The time-averaged scale heights of the two GRMHD simulations are shown in Figure 11. This code evolves the internal energy equation, rather than the total energy equation, and its simulations did not employ an explicit cooling function. Rather, entropy is conserved except where local shock heating is captured by an artificial viscosity term. Thus, the scale height is not controlled directly and is determined primarily by the initial condition. In the end, the two simulations have very similar scale-height profiles, with $H/R \simeq 0.15$ for $r \geqslant 10M$, but declining inward, reaching $\simeq$0.12 at the ISCO ($r = 6M$) and $\simeq$0.06 just outside the horizon. The mean H/R for both is $\simeq$0.14.

4. RESULTS: STRESS IN THE INNER DISK

With this background in mind, we can now discuss the results for time-averaged stress in the inner disk. We will present them in two ways: in terms of the radial profile of the spherical shell-integrated fluid-frame electromagnetic stress, and in terms of the angular momentum flux and the quantity $j_{\rm net}$ defined in the introduction.

4.1. Fluid-frame Electromagnetic Stress Profile

We begin with the radial profile of the electromagnetic stress. Both for the purpose of highlighting the physics and for the purpose of contrasting with the Novikov–Thorne model, it is best to compute it in the fluid frame

$$W^{(r)}_{(\phi)}(r) = \frac{\int\int dx^{(\phi)} dx^{(\theta)} \left(|b|^2 u^\nu u_\mu - b^\nu b_\mu\right) e^{(r)}_\nu e^\mu_{(\phi)}/(4\pi)}{\int dx^{(\phi)}|_{\theta=\pi/2}}, \tag{12}$$

where b^μ is the magnetic 4-vector. Each component of the vector $dx^{(\mu)} = e^{(\mu)}{}_\nu\, dx^\nu$ represents the extent of a cell's dimension as measured in the fluid element's rest frame, and $e^{(\mu)}{}_\nu$ is the orthonormal tetrad that transforms vectors in the Boyer–Lindquist coordinate frame to the local fluid frame (see Beckwith et al. 2008b for explicit expressions for the tetrad). The vector dx^ν is the Boyer–Lindquist coordinate frame version of the Kerr–Schild vector $dx^\nu_{\rm KS} = [0, \Delta r, \Delta\theta, \Delta\phi]\,(r, \theta, \phi)$, where Δr, $\Delta\theta$, and $\Delta\phi$ are, respectively, the radial, poloidal, and azimuthal extents of our simulation's finite volume cell located at (r, θ, ϕ).[7]

The physical significance of the electromagnetic fluid-frame stress profile is that it describes the rate at which angular momentum is carried outward by electromagnetic fields. The net angular momentum accreted by the black hole is diminished to the degree that stresses like these convey angular momentum outward even while inflowing matter carries its orbital angular momentum inward. The Novikov–Thorne model assumes that the stress begins to decline outside of the ISCO, reaching zero at that point. Agol & Krolik (2000) showed how changing that boundary condition to account for nonzero stress at the ISCO, i.e., $j_{\rm net} < u_\phi$(ISCO), could significantly alter the shape of the stress profile. Even in the disk body, well outside the ISCO, a smaller $j_{\rm net}$ can lift the time-averaged stress above the Novikov–Thorne curve.

Figure 12 shows the time-averaged $W^{(r)}_{(\phi)}(r)$ for each of the HARM3D simulations, normalized by their time-averaged accretion rate. The dotted line shows the Novikov–Thorne prediction and the dot-dash curves are examples of an Agol–Krolik profile (Agol & Krolik 2000). Remarkably, all five of the HARM3D simulations show almost identical profiles, differing only in very minor ways. We concentrate on the region where inflow equilibrium applies, here $r \leqslant 20M$. Outside the ISCO,

[7] Care must be exercised to properly evaluate volume integrals in the fluid frame. Both Krolik et al. (2005) and Shafee et al. (2008) correctly projected the stress tensor into the fluid frame, but failed to similarly project the volume element.

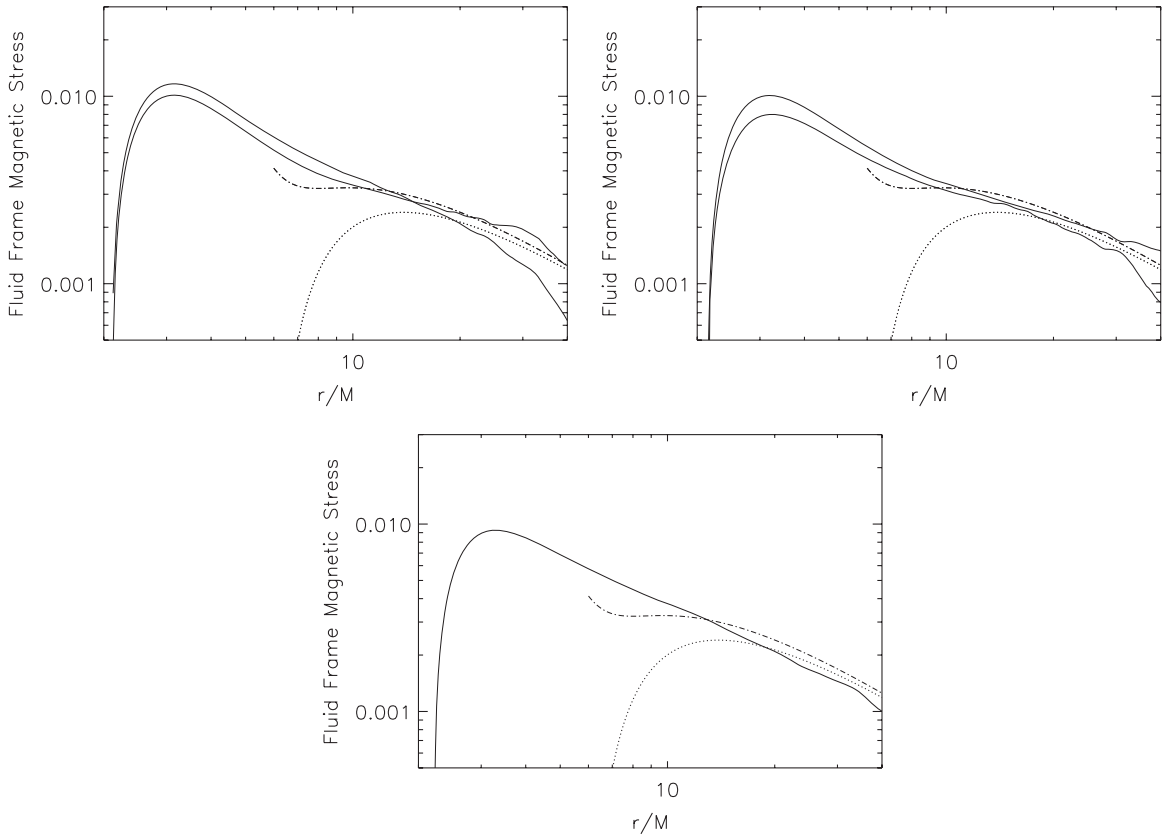

Figure 12. Fluid-frame electromagnetic stress, normalized by that simulation's mean accretion rate, for each of the disk aspect ratios. Top left: ThinHR and ThinLR; top right: MediumHR and MediumLR; bottom: ThickHR. Heavy and light curves correspond respectively to HR and LR. Dotted curves show the Novikov–Thorne model's prediction, dot-dashed curves the prediction of the Agol–Krolik model with additional efficiency $\Delta\epsilon = 0.015$—a 26% increase relative to the Novikov–Thorne efficiency $\epsilon = 0.057$.

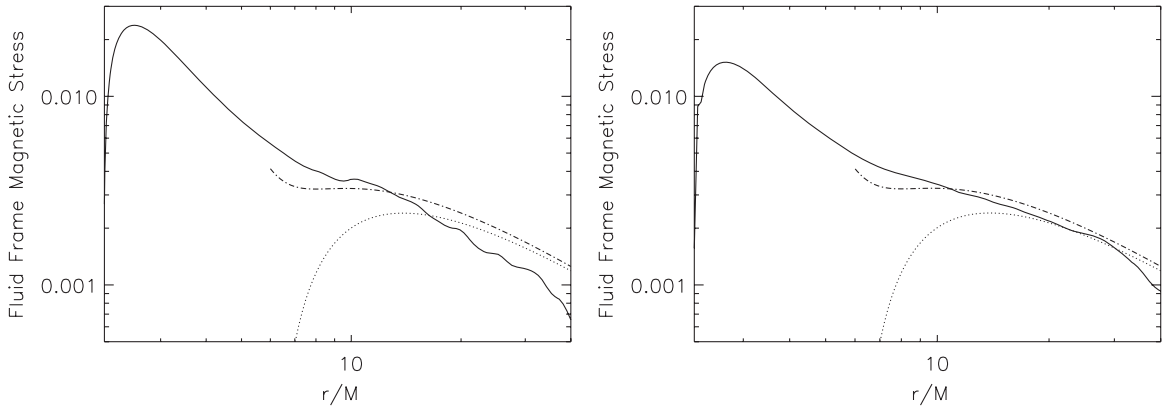

Figure 13. Fluid-frame electromagnetic stress, normalized by that simulation's mean accretion rate, for the GRMHD simulations. Left: KD0c. Right: VD0. Curve identifications are as in Figure 12.

but inside the domain of inflow equilibrium, the fluid-frame stress usually (but not always) lies slightly above the Novikov–Thorne prediction. Although the match is not perfect, it is somewhat better described by the Agol–Krolik model. As the flow approaches the ISCO, where the Novikov–Thorne model would predict that the stress begins to fall, the electromagnetic stress rises steadily. Inside the ISCO, in the plunging region, the stress continues to rise inward, with a slope that is similar to or slightly steeper than outside the ISCO. Just outside the event horizon, the stress falls sharply to zero: because this stress component is nothing more than the radial flux of angular momentum of rotation in the disk plane, when the black hole has no angular momentum (i.e., does not rotate), it cannot act as a source of angular momentum and the stress immediately outside it must go to zero.

The corresponding profiles for the two GRMHD simulations are shown in Figure 13. They are very similar to one another, and qualitatively similar to, but quantitatively different from, the HARM3D profiles. Like the HARM3D profiles, the radial slope of the stress is nearly constant in the disk outside the ISCO; unlike the HARM3D profiles, in these two the stress rises somewhat *more* steeply inside the ISCO. As a result, the peak stress in these two simulations is $\simeq$2 times greater than seen in the HARM3D cases.

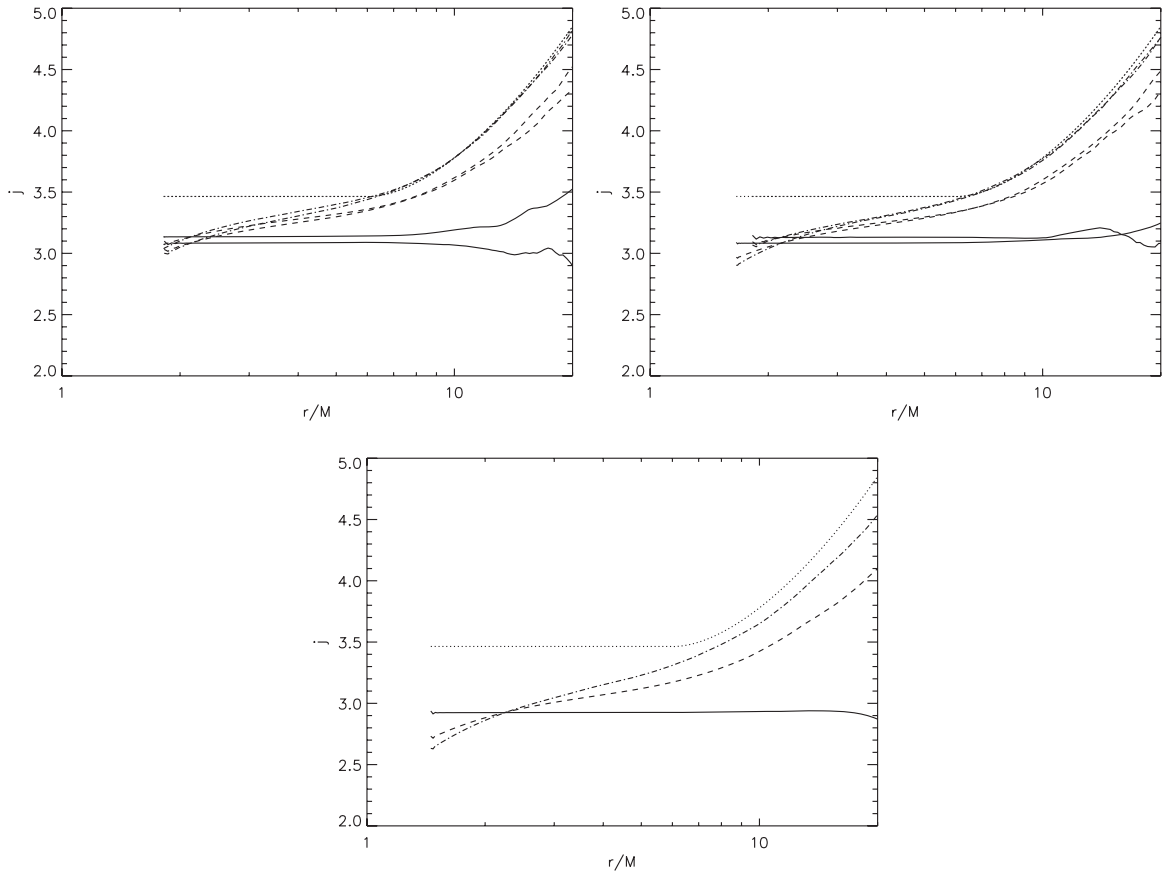

Figure 14. Accreted angular momentum per unit rest mass for each of the three aspect ratios simulated with HARM3D. Top left: ThinHR and ThinLR; top right: MediumHR and MediumLR; bottom: ThickHR. Solid curves show $j_{\rm net}$, with the heavy curves corresponding to HR and the light curves to LR. Dotted curves show the angular momentum of a circular orbit as a function of radius; inside the ISCO, it is held constant at u_ϕ(ISCO), consistent with the Novikov–Thorne model. Dashed curves represent the time-averaged specific angular momentum carried by the accreting matter, i.e., $\langle \rho h u^r u_\phi \rangle / \langle \rho u^r \rangle$. Dot-dashed curves are the time-averaged mass-weighted mean angular momentum at each radius, i.e., $\langle \rho h u_\phi \rangle / \langle \rho \rangle$.

In conclusion, despite the range of temperatures and scale heights covered by these models, there is a great similarity between the stress profiles of all the HARM3D models as well as KD0c and VD0. In other words, with respect to this measure of the stress, there appears to be no dependence on H/R whatsoever.

Furthermore, the similarity between KD0c and VD0 suggests that the change of magnetic topology from closed dipolar loops on the scale of the disk thickness to net vertical field also makes little difference to the radial variation of accretion stress. One possible explanation for this insensitivity is the fact that reconnection events in the corona largely decoupled the magnetic field in the inner disk of VD0 from the large-scale flux (Beckwith et al. 2009). The remaining field in the disk then has a topology not so different from that in the other simulations. In Section 5, we review the results from previously published simulations to explore further the possible role of field topology on ISCO stress.

4.2. Specific Accreted Angular Momentum

The value of $j_{\rm net}$, the mean angular momentum accreted per unit rest mass, summarizes the net angular momentum flow in the system. It is determined by several effects. In the accretion disk body, the orbital angular momentum, u_ϕ, is close to the value associated with a circular test-particle orbit at that radius, but can be altered by an amount $\sim(H/R)^2$ by radial pressure gradients, both gas and magnetic. Stresses, both electromagnetic (Maxwell) and fluid (Reynolds) move angular momentum through the accretion flow; to the degree that they have a net divergence, they can either add or remove angular momentum from the fluid. In the classical Novikov–Thorne model, the fluid's angular momentum is *assumed* to match the local circular orbit angular momentum at all locations outside the ISCO, but is fixed at the ISCO angular momentum at all smaller radii. The stresses, whether Maxwell or Reynolds, are constrained to be exactly what they need to be to produce this result: finite in the disk body, zero in the plunging region. As a result, $j_{\rm net}$ is predicted to be exactly u_ϕ(ISCO).

As can be seen from the data listed in Table 2, this is not the case in the simulations. We find that, over the range of thicknesses and magnetic geometries studied, $j_{\rm net}$ ranges from $\simeq$2.93 to $\simeq$3.21. Thus, in all these cases, the accreted angular momentum per unit accreted rest mass is 7%–15% below u_ϕ(ISCO) = 3.464. Interestingly, the largest $j_{\rm net}$ by far was seen in KD0c, a simulation performed on a comparatively coarse grid; if it were discounted, the depression of $j_{\rm net}$ below u_ϕ would be 10%–15%.

The separate elements contributing to this departure from the Novikov–Thorne prediction are shown by the curves in Figures 14 and 15. The solid lines correspond to the net specific angular momentum flux; in inflow equilibrium this should be constant with radius. The dashed curves show the time-averaged specific angular momentum carried by the accreting matter, i.e.,

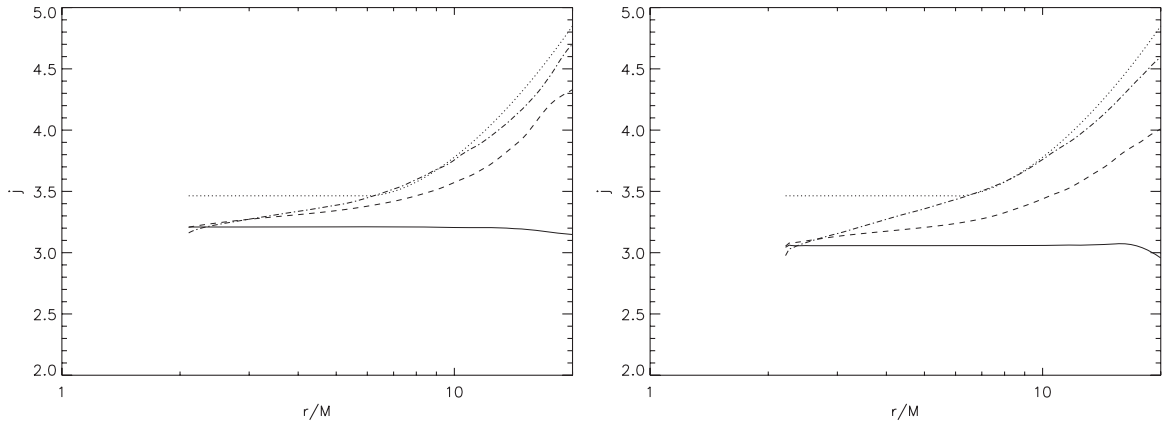

Figure 15. Accreted angular momentum per unit rest mass for the two GRMHD simulations. Left: simulation KD0c. Right: simulation VD0. Curves have the same identifications as in Figure 14.

$\langle \rho h u^r u_\phi \rangle / \langle \rho u^r \rangle$. The difference between these curves and the net angular momentum flux is due to the electromagnetic stress. The dot-dash curves show the time-averaged mass-weighted mean angular momentum at each radius, $\langle \rho h u_\phi \rangle / \langle \rho \rangle$. These last two quantities can be compared with the u_ϕ corresponding to a circular orbit, shown by the dotted line (which is held constant at the ISCO value inside of that radius).

For all the models, the mass-weighted mean angular momentum generally follows the circular orbit value outside of the ISCO, but continues to decline inside of that radius rather than holding steady. In the thin disk models the offset from the circular orbit value is small, while in the thicker cases this offset is somewhat larger. This is precisely what one would expect; the gas in the disk is partially supported by the outward radial decline in pressure, primarily magnetic, in disks with a larger H/R.

In every case, the curve of mean angular momentum accreted by the matter lies well below the curve of the local mass-weighted mean angular momentum. One way to view the origin of this offset stems from the fact that the material in the disk is turbulent; local fluid elements have angular momenta that fluctuate from time to time and from place to place. It should be no surprise that fluid elements with angular momentum slightly smaller than the value that would support a local circular orbit tend to move inward faster than those with larger angular momentum. In other words, the mean-accreted angular momentum is systematically biased toward lower values by orbital mechanics that sorts the fluid elements according to their place in the local angular momentum distribution.

This effect can also be identified with turbulent Reynolds stress. To see this identification directly, consider the equation of angular momentum equilibrium integrated over spherical shells and averaged in time

$$\langle \rho h u^r u_\phi \rangle + \langle M^r_\phi \rangle = j_{\rm net} \langle \rho u^r \rangle, \tag{13}$$

where M^r_ϕ is the Maxwell stress. The term $\propto u^r u_\phi$ can be broken into two pieces, one reflecting the advection of the mean angular momentum (weighted by enthalpy) and the other reflecting departures from the mean. Dividing through by the mass accretion rate, the previous equation becomes

$$\langle h u_\phi \rangle - \frac{\langle \delta(\rho u^r) \delta(h u_\phi) \rangle + \langle M^r_\phi \rangle}{-\langle \rho u^r \rangle} = j_{\rm net}, \tag{14}$$

where $\delta X \equiv X - \langle X \rangle$. That is, the net rate at which angular momentum is carried inward per unit rest mass accreted is the local mean angular momentum reduced by the ratio of the total stress, Maxwell plus turbulent Reynolds, to accretion rate. Comparing this formalism to Figures 14 and 15, we see that the dot-dashed curves show $\langle \rho h u_\phi \rangle / \langle \rho \rangle \simeq \langle h u_\phi \rangle$, while the dashed curves show $\langle \rho h u^r u_\phi \rangle / (-\langle \rho u^r \rangle)$. Their offset can then be attributed to the turbulent Reynolds stress normalized to the accretion rate, $\langle (\delta \rho u^r) \delta (h u_\phi) \rangle / (-\langle \rho u^r \rangle)$. This turbulent Reynolds stress can be quantitatively significant, particularly in VD0 and to a lesser degree in ThickHR.

The separation between the curve of the accretion-weighted mean angular momentum and $j_{\rm net}$ is the electromagnetic angular momentum flux, and in every simulation but VD0 it clearly makes the largest contribution to the outward angular momentum flux. In all the other cases, the only place where the Maxwell stress does not outweigh the Reynolds stress is in the immediate vicinity of the event horizon. There, the matter's angular momentum flux becomes almost exactly the total because a nonspinning black hole has no angular momentum to lose. For the same reason, just outside the horizon $||b||^2 u^r u_\phi$ comes to exceed $b^r b_\phi$ in magnitude, and the net electromagnetic angular momentum flux turns (weakly) negative.

To conclude, then, all these models show values of $j_{\rm net}$ that are reduced below the ISCO value, regardless of H/R. The electromagnetic stress in the fluid frame hardly varies at all from one simulation to the next; consequently, its contribution to the net angular momentum flux is likewise nearly the same in all cases. Scale height does seem to have an effect on the run of u_ϕ through the disk: u_ϕ is reduced below the circular orbit value in proportion to the magnitude of radial pressure support. It also appears that the Reynolds stress levels may be partially controlled by the scale height in the disk and partially by the magnetic topology.

5. REVIEW OF PREVIOUS SIMULATIONS

In this section, we summarize some results from previous simulations. Some of these, although not designed specifically to study the influence of scale height, can nevertheless provide additional information about how the inner disk stress depends on other parameters, notably magnetic field topology. Others are more directly comparable to our HR series of simulations.

We have already discussed models KD0c (Krolik et al. 2005) which began with simple dipole loops in the initial torus, and VD0 (Beckwith et al. 2009), a model that began with a vertical field piercing the initial torus. Beckwith et al. (2008a) feature three simulations all computed in a Kerr ($a/M = 0.9$) spacetime

with identical fluid initial states, but differing initial magnetic fields: in KDPg, the field configuration was nested dipolar loops similar to those in KD0c; in QDP, there was a pair of quadrupolar field loops above and below the equator whose associated currents had opposite signs; and in TDPa, the initial condition held only toroidal field.

Figure 2 of Beckwith et al. (2008a) provides data for investigating how these different initial field configurations affect inner disk stress. Panel (f) shows the coordinate-frame electromagnetic angular momentum flux (shell- and time-averaged $T^r_\phi(EM)$) as a function of radius. The curves for KDPg and QDPa, the large dipolar field and quadrupolar simulations, are nearly identical. Both curves are generally a factor of several higher than that of TDPa, the one whose initial field was purely toroidal. Figure 2(c) of Beckwith et al. (2009) shows the radial run of net specific angular momentum (what we call $j_{\rm net}$ here, but is labeled L in that figure). Both KDPg and QDPa are slightly below (by $\simeq$0.05) the ISCO value of 2.1. TDPa, on the other hand, has an average-accreted specific angular momentum of 2.13, very nearly the exact ISCO angular momentum, when averaged over the last $9000M$ in time. The similarity between quadrupole and dipole initial fields carries over to simulations with a Schwarzschild hole. Another GRMHD simulation, QD0 (described in Beckwith et al. 2008b), also has quadrupolar loops in the initial torus. It was run for 10^4M in time, and averaging over the last $2000M$ in time gives a value of $j_{\rm net} = 3.21$ for the specific angular momentum accreted into the hole, similar to KD0c. As a whole, these results suggest that the crucial distinction may be between a field with significant poloidal character (either with or without net flux) and one that is only toroidal.

There is another case where we can clearly see the significance of a particular field configuration. The vertical field model VD0 was evolved in both two and three dimensions (Beckwith et al. 2009). In the present context, the contrast between the two is interesting (see Figure 7 of Beckwith et al. 2009). In the axisymmetric simulation, the value of $j_{\rm net}$ shows strong fluctuations. Between the times of 10^4M and 1.5×10^4M (the end of this simulation), the mean of $j_{\rm net}$ is 2.85, but with a standard deviation of 0.43. Values as low as $\sim$1.0 are reached at particular moments. The mean value of $j_{\rm net}$ over the same interval in VD0 is similar, 2.89, but the standard deviation is only 0.18 and the minimum value reached is 2.43. Axisymmetric simulations with vertical fields typically show strong MRI "channel modes" characterized by extended radial flows accompanied by radial magnetic field. It is the presence of those extended radial fields through the plunging region that provide the strong torques. Thus, the two-dimensional simulation illustrates the basic principle obtaining in three dimensions, but in exaggerated form. In this particular case, the presence of a net vertical field (which cannot be reconnected away within the disk) also prevents the antidynamo effect from dissipating the turbulence, allowing the stress in the plunging region to remain over the full evolution.

Our HARM3D simulations are very close, both in numerical technique and parameters, to the general relativistic MHD simulation of Shafee et al. (2008). The Shafee et al. simulation was done, like ours, in the context of a nonrotating black hole. Both employed intrinsically conservative Godunov algorithms differing in only minor respects. Shafee et al. used a temperature regulation scheme based on maintaining constant entropy rather than a target temperature, but—compared to our ThinHR simulation—the resulting aspect ratio was only slightly thicker in the mean and somewhat less constant as a function of radius.

In their initial hydrodynamic conditions, our HR simulations were almost identical to those of Shafee et al., differing only in the q parameter (theirs was chosen to give an initial state with $H/R \simeq 0.1$, ours had variously $H/R \simeq 0.05$, 0.08, and 0.16). However, they did differ in the initial state of the magnetic field. Whereas our initial magnetic field was a set of nested dipole loops centered on the pressure maximum, they imposed two sets of loops, centered on $r = 28M$ and $r = 38M$, which they then perturbed randomly with $\simeq$50% fractional amplitude.

The spatial grid used by Shafee et al. was also very similar to the one we employed for ThinHR. They used a grid with $512 \times 128 \times 32$ cells, whereas ThinHR used $912 \times 160 \times 64$ cells. Both radial grids were logarithmic, but their grid extended to a slightly smaller radius than ours ($50M$ as opposed to $70M$); their radial cell size was therefore about 1.6 times larger than ours. The polar-angle grid scheme for ThinHR was finer than that of Shafee et al. near the equator, resulting in $\simeq$30% more cells per scale height. The two simulations had identical azimuthal resolutions because, even though we used twice as many cells, our azimuthal extent was also twice as great ($\pi/2$ as opposed to $\pi/4$). Shafee et al. reported that in their initial condition, there were $\sim$10 cells per fastest growing MRI wavelength, but do not say how that number changed during the simulation.

Despite this very close similarity, Shafee et al. arrived at a result that was quite different from ours. They found that the fluid-frame electromagnetic stress followed the Novikov–Thorne prediction very closely all the way to $r = 9M$, and then maintained more or less that amplitude all the way to $r \simeq 2.5M$. In contrast, as Figure 12 shows, in ThinHR (and all our other simulations), the fluid-frame electromagnetic stress is tens of percent above the Novikov–Thorne prediction in the disk body, and rises steeply inward inside $r = 10M$, reaching a level $\simeq$5 times greater than the stress found in the Shafee et al. calculation. Similarly, although we found $u_\phi(\mathrm{ISCO}) - j_{\rm net} \simeq 0.33$, Shafee et al. found a value less than half as large, only $\simeq$0.14.

The origin of this contrast is uncertain. Although we have not yet performed a simulation with several dipolar loops, the very minor contrast between Kerr simulations with dipolar and quadrupolar initial field suggests that different forms of poloidal field are not, by themselves, significant. However, different field structures can place different demands on spatial resolution; as clearly demonstrated by MediumLR (and perhaps by KD0), inadequate resolution can lead to substantial artificial suppression of magnetic field strength. The figures illustrating results from MediumLR that we have shown in this paper all draw on data from the period during that simulation when it remained well resolved; at later times, as its resolution quality failed, its electromagnetic stresses steadily weakened and $u_\phi(\mathrm{ISCO}) - j_{\rm net}$ diminished. Because it entails more small-scale structure, a pair of dipole loops, as in the Shafee et al. initial condition, may create a turbulent magnetic field more vulnerable to reconnection than our single dipolar loop, particularly when perturbed by 50% and studied with a grid having larger radial cells.

It is possible that two other considerations may also play a role in creating these contrasting conclusions. First, their simulation ran only to a time of $10000M$, and they presented no data demonstrating how well, and over what range of radii, it reached a state of inflow equilibrium. Because we found that a disk of this thickness takes $\simeq 10000M$ to reach equilibrium, their shorter duration may be problematic. Second, the Shafee et al. simulation had an azimuthal range of only $\pi/4$. Schnittman et al. (2006) showed that the characteristic azimuthal coherence

length of features in full 2π global disk simulations was $\simeq$1 rad. This result suggests that an azimuthal extent of only $\pi/4$ might misrepresent the MHD turbulence.

6. DISCUSSION

It is almost 20 years since the first recognition (Balbus & Hawley 1991) that magnetic fields can produce significant stress with disks; it has been 10 years since the first suggestions (Krolik 1999b; Gammie 1999) that this stress could continue within the ISCO, with implications for the overall efficiency and luminosity of accretion disk. However, there remains controversy about how large these effects may be and how they depend on disk parameters. Because the first general relativistic MHD accretion simulations demonstrated that these stresses are significant in disks with thickness $H/R \simeq 0.15$ (Krolik et al. 2005), the discussion in the last several years has centered on whether they might diminish with decreasing disk thickness (Reynolds & Fabian 2008; Shafee et al. 2008). In this paper, we have carried out a series of simulations carefully designed to isolate the effect of varying H/R; we find in all of our simulations that the electromagnetic fluid-frame stress increases steeply inward almost all the way to the event horizon. Indeed, even for a contrast of a factor of 3 from the thickest to the thinnest disk, we find an almost imperceptibly small change in the fluid-frame electromagnetic stress profile. The most natural interpretation of our results is that the radial distribution of electromagnetic stress depends at most only weakly on disk thickness. In our simulations, these stresses diminish $j_{\rm net}$, the net angular momentum per unit rest-mass accreted, by $\sim$10%. This result supports quantitatively the very crude qualitative argument given in Krolik (1999b) that the Alfvén speed in the plunging region would always become marginally relativistic, more or less independent of the accretion rate, so that magnetic stresses there would always be significant, but would always be dominated by gravitational forces.

It is also in keeping with other lines of qualitative reasoning. One might begin by asking, "If stirring of MHD turbulence by the MRI leads to significant magnetic stresses in the disk body, what might change near the ISCO?" As shown by Gammie & Popham (1998), the orbital shear in the plunging region in a Kerr spacetime differs from the Newtonian value by only a number of order unity. Consequently, if the magnetic pressure continues to be smaller than the gas pressure in the disk's equatorial plane, one would expect linear growth of the MRI to behave in very much the same way as in the disk body. If the gas pressure falls relative to the magnetic pressure so that the plasma β drops below unity, thereby quenching linear growth of the MRI, then magnetic stresses are surely important. However, nonlinear development of the turbulence can be expected to change as the infall time becomes as short or shorter than the eddy turnover time, the time for the energy of turbulent motions to move from long length scales to short. Indeed, earlier work (Hirose et al. 2004) has shown that the magnetic field becomes both much smoother and somewhat less tightly wound (i.e., the radial component grows somewhat relative to the toroidal component) just inside the ISCO. Such a change in structure could alter both the rate of field amplification and the rate of field dissipation. On the basis of simple arguments like these, however, it is difficult to say whether these changes should lead to a larger or smaller mean field intensity and therefore stress. In the limit that both amplification and dissipation become weaker, flux-freezing results in growing magnetic stresses (Krolik 1999b; Gammie 1999). Moreover, with the principal dynamics—orbital shear and a growing radial velocity—all acting in the equatorial plane, there is no obvious place for a dependence on disk thickness.

This physical argument is bolstered by the fact that the different simulation versions differ only slightly. Significantly different grid schemes, contrasting initial conditions, and even wholly different codes make only slight differences in the outcome. Even the topological contrast of substantial net vertical flux versus none at all seems to change the stress by only a modest amount.

On the other hand, we have also found that fluid effects in the inner disk can also contribute to a diminution in $j_{\rm net}$. Pressure support of the matter in the disk is, by definition, proportional to $(H/R)^2$. Consequently, the mass-weighted mean angular momentum at any location in the disk is smaller than the angular momentum of a test particle at that radius by a comparable amount. More significantly, Reynolds stresses can reduce it further, by an amount that increases both with increasing disk thickness and with net magnetic flux trapped on the horizon.

A few notes of caution should be injected into this discussion, however, previous work studying accretion in a Kerr ($a/M = 0.9$) geometry (Beckwith et al. 2008a) suggests that a disk magnetic field that has no net poloidal content might produce weaker electromagnetic stress both throughout the disk and in the ISCO region. This effect should be explored more thoroughly in future work. We have also shown that before interpreting simulation results in terms of their implications for steady-state accretion, it is important to check carefully both that the simulation approximates inflow equilibrium and that the simulation's spatial grid provides adequate resolution throughout the period studied.

We conclude, then, that there appears to be little evidence for a strong dependence of near-ISCO electromagnetic stress on either disk thickness or the net magnetic flux. Because disk thickness is really a function of accretion rate, substantial near-ISCO electromagnetic stress should be seen in black hole accretion systems whether they are accreting at a rate near Eddington or far below. Its weak dependence on net magnetic flux suggests that the impact of electromagnetic stresses should be similarly independent of external magnetic boundary conditions. At the same time, we also find a supplemental reduction of the net accreted angular momentum due to Reynolds stresses, and this depends on both H/R and magnetic geometry. When the Reynolds stress is weakest, so only the near-universal electromagnetic stress acts, $j_{\rm net}$ is reduced below u_ϕ(ISCO) by $\simeq$7%–10%; when the Reynolds stress is strongest, the reduction is as large as 15%.

Fully quantitative conclusions, however, await several extensions of this work: to rotating black holes, to disks with more complex magnetic topologies, and to disks whose scale heights are constant, rather than proportional to radius. In the radiation-dominated regime (which should apply to the inner regions of accretion disks around black holes whenever the accretion rate is near Eddington, particularly when the central mass is large: Shakura & Sunyaev 1973), H is constant as a function of radius. Therefore, a flat-topped disk is a more realistic model for disks as we are likely to find them in nature. All of these extensions should be feasible in the near term.

This work was supported by NSF grant AST-0908869 and NASA grant NNX09AD14G (J.F.H.), and by NSF grant AST-0507455 (J.H.K.). Some of the simulations described were carried out on the Teragrid Ranger system at TACC and

the Teragrid Abe system at NCSA, both supported by the National Science Foundation. Other simulations were run on the Johns Hopkins Homewood High-Performance Computing Center cluster.

REFERENCES

Abramowicz, M. A., Lanza, A., & Percival, M. J. 1997, ApJ, 479, 179
Afshordi, N., & Paczyński, B. 2003, ApJ, 592, 354
Agol, E., & Krolik, J. H. 2000, ApJ, 528, 161
Balbus, S. A., & Hawley, J. F. 1991, ApJ, 376, 214
Balbus, S. A., & Hawley, J. F. 1998, Rev. Mod. Phys., 70, 1
Beckwith, K., Hawley, J. F., & Krolik, J. H. 2008a, ApJ, 678, 1180
Beckwith, K., Hawley, J. F., & Krolik, J. H. 2008b, MNRAS, 390, 21
Beckwith, K., Hawley, J. F., & Krolik, J. H. 2009, ApJ, 707, 428
Davis, S. W., Stone, J. M., & Pessah, M. E. 2009, arXiv:0909.1570
De Villiers, J.-P., & Hawley, J. F. 2003, ApJ, 589, 458
De Villiers, J.-P., Hawley, J. F., & Krolik, J. H. 2003, ApJ, 599, 1238
Fromang, S., & Papaloizou, J. 2007, A&A, 476, 1113
Gammie, C. F. 1999, ApJ, 522, L57
Gammie, C. F., McKinney, J. C., & Tóth, G. 2003, ApJ, 589, 444
Gammie, C. F., & Popham, R. 1998, ApJ, 498, 313
Gammie, C. F., Shapiro, S. L., & McKinney, J. C. 2004, ApJ, 602, 312
Hawley, J. F., & Krolik, J. H. 2001, ApJ, 548, 348
Hawley, J. F., & Krolik, J. H. 2002, ApJ, 566, 164
Hawley, J. F., & Krolik, J. H. 2006, ApJ, 641, 103
Hirose, S., Krolik, J. H., De Villiers, J.-P., & Hawley, J. F. 2004, ApJ, 606, 1083
Krolik, J. H. 1999a, Active Galactic Nuclei: From the Central Black Hole to the Galactic Environment (Princeton, NJ: Princeton Univ. Press)
Krolik, J. H. 1999b, ApJ, 515, L73
Krolik, J. H., Hawley, J. F., & Hirose, S. 2005, ApJ, 622, 1008
Machida, M., & Matsumoto, R. 2003, ApJ, 585, 429
Noble, S. C., Gammie, C. F., McKinney, J. C., & Del Zanna, L. 2006, ApJ, 641, 626
Noble, S. C., Krolik, J. H., & Hawley, J. F. 2009, ApJ, 692, 411
Noble, S. C., Leung, P. K., Gammie, C. F., & Book, L. G. 2007, Class. Quantum Grav., 24, 259
Novikov, I. D., & Thorne, K. S. 1973, in Black Holes (Les Astres Occlus), ed. C. DeWitt & B. S. DeWitt (New York: Gordon and Breach), 343
Page, D. N., & Thorne, K. S. 1974, ApJ, 191, 499
Reynolds, C. S., & Armitage, P. J. 2001, ApJ, 561, L81
Reynolds, C. S., & Fabian, A. C. 2008, ApJ, 675, 1048
Sano, T., Inutsuka, S.-i., Turner, N. J., & Stone, J. M. 2004, ApJ, 605, 321
Schnittman, J. D., Krolik, J. H., & Hawley, J. F. 2006, ApJ, 651, 1031
Shafee, R., McKinney, J. C., Narayan, R., Tchekhovskoy, A., Gammie, C. F., & McClintock, J. E. 2008a, ApJ, 687, L25
Shakura, N. I., & Sunyaev, R. A. 1973, A&A, 24, 337
Shi, J.-M., Krolik, J. H., & Hirose, S. 2010, ApJ, 708, 1716
Thorne, K. S. 1974, ApJ, 191, 507